Tracking Microstructure Evolution in Complex Biaxial Strain Paths: A Bulge Test Methodology for the Scanning Electron Microscope

As Published: https://doi.org/10.1007/s11340-019-00538-8

Publisher: Springer US

Persistent URL: https://hdl.handle.net/1721.1/131890

Version: Author's final manuscript: final author's manuscript post peer review, without publisher's formatting or copy editing

Tracking microstructure evolution in complex biaxial strain paths: A bulge test methodology for the scanning electron microscope.

Cite this article as: E. Plancher, K. Qu, N. H. Vonk, M. B. Gorji, T. Tancogne-Dejean, C.C. Tasan, Tracking microstructure evolution in complex biaxial strain paths: A bulge test methodology for the scanning electron microscope., *Experimental Mechanics*, doi: 10.1007/s11340-019-00538-8

Tracking microstructure evolution in complex biaxial strain paths: A bulge test methodology for the scanning electron microscope.

E. Plancher[1,*], K. Qu[1], N. H. Vonk[1], M. B. Gorji[2], T. Tancogne-Dejean[2], C.C. Tasan[1,*]

[1] Massachusetts Institute of Technology, Department of Materials Science and Engineering,

77 Massachusetts Avenue, Cambridge, MA 02139, USA

[2] Massachusetts Institute of Technology, Department of Mechanical Engineering,

77 Massachusetts Avenue, Cambridge, MA 02139, USA

*Corresponding authors (emeric.plancher@mines-saint-etienne.org, tasan@mit.edu)

Abstract

In this work, a novel method is presented to track site-specific microstructure evolution in metallic materials deformed biaxially along proportional and complex strain paths. A miniaturized bulge test setup featuring a removable sample holder was designed to enable incremental measurements to be performed in a scanning electron microscope, by probing the same position on the sample at different deformation levels, with electron backscatter diffraction (EBSD), electron channeling contrast imaging (ECCI) and other imaging modes. Validation experiments were performed at room temperature on samples prepared from commercial sheet metal (dual-phase steel) and foils (stainless steel). Local strain measurements with the digital image correlation technique confirmed that proportional strain paths with a strain ratio up to 5 can be investigated using elliptical dies in the bulge test holder. It is also shown how complex strain paths can be obtained using a combination of overlapping elliptical dies. Incremental EBSD and ECCI were conducted in configurations relevant for the multi-scale investigation of localized plasticity and damage mechanisms in dual-phase steel. Quantitative information regarding microstructure evolution (phase fractions, orientation fields, dislocation structures, etc.) and regarding local strain distributions could be successfully obtained. This type of data sheds light on underlying deformation mechanisms and provides opportunities to calibrate crystal plasticity models.

Keywords: biaxial loading; SEM; EBSD; ECCI; micro-mechanics

1. Introduction

One of the core challenges in the design of structural alloys is to achieve optimal combinations of strength, toughness and ductility. The general trend to overcome this challenge is to design metals with complex microstructures containing multiple phases with contrasted mechanical properties. Examples are numerous: dual phase steels, duplex stainless steels, $\alpha+\beta$ titanium alloys, nickel-based superalloys, cobalt alloys, etc. These alloys can be engineered to have a wide range of microstructure characteristics (e.g. phase volume fractions, morphologies, sizes, distributions), creating a vast spectrum for microstructure design. However, the assembly of phases with contrasted properties leads, during deformation, to microscale stress-strain localization and damage phenomena that depend on the local stress state, the strain path followed [1–5] and the presence of strain path changes [6–9]. As microstructural damage often leads to premature necking or failure at the macro-scale [10–15], those phenomena are of specific importance in sheet metal forming. Some plasticity mechanisms such as deformation-induced phase transformation (TRIP effect) are also strongly affected by the deformation mode and strain changes [16–18]. There is thus a great interest to develop experimental methods that would allow linking complex loading conditions to simultaneous measurements of mechanical and microstructural fields (i.e. multi-field mapping), with the goal to shed light on the link between plasticity, damage mechanisms and microstructure characteristics. To this end, important experimental requirements are: (i) having a tool with a range of analytical techniques that combine mapping capabilities with high spatial resolution (to capture, e.g., damage nucleation processes) and large field-of-view (to capture long-range 'neighborhood' effects); and (ii) using the proper deformation stage to impose mechanical boundary conditions on the sample in a controlled manner.

Regarding the first challenge, scanning electron microscopes (SEM), which enable measurements with both high spatial resolution (< 10 nm) and large field-of-view (~mm^2), are ideal choices. Analytical SEM techniques such as electron backscatter diffraction (EBSD) [19] and electron channeling contrast imaging (ECCI) [20] provide valuable new insights into local defect evolution [21], plastic strain fields [22,23], intragranular elastic strain fields [24–26],

boundary damage mechanisms [27] and micro-crack microstructure interactions [28]. Employing digital image correlation (DIC) on SEM images [29,30], quantitative evaluation of microscopic strains can be measured, most accurately by employing submicron-sized artificial patterns [31,32]. Coupling DIC and emerging absolute high angular resolution EBSD (to evaluated local stress fields) [33,34] has the potential to give access to a direct measurement of the local behavior as in experiments using synchrotron techniques [35]. When applied *in situ* during deformation experiments, EBSD and DIC have been used to track microstructural evolutions and related local strain fields [36,37].

To address the second challenge, a variety of *in situ* SEM deformation stages have been developed to explore different deformation modes [38]: e.g., uniaxial tension [10,39–41], biaxial tension [28,42,43], shear deformation [44]. However, regardless of how miniaturized such setups are, once installed in the SEM chamber, the geometrical requirements of different imaging modes (e.g. EBSD, ECCI, or in-lens SE for DIC [32]) become a challenge in a multi-field mapping approach where several techniques have to be employed consecutively. In commercial uniaxial straining stages, EBSD can be performed by employing 70° pre-tilted clamps or tilting the SEM stage. The latter requires specific EBSD camera positions and large working distances. In either case, switching back to e.g. in-lens SE mode (0°) or ECCI mode (<~10°, with a short working distance) is not practical. The case of biaxial straining is even more challenging due to the complexity of required deformation setups. For cruciform-type geometries with two independent loading axes, low tilt angles are typically employed for EBSD measurements (*e.g.* 58° [45]). An alternative approach is to design a mechanism that imposes an equi-biaxial loading from a single loading axis [28]. A miniaturized Marciniak test setup provides the cleanest multi-axial deformation state[1], however; with this setup, *in situ* EBSD is not possible [42]. Given all these limitations, new methods are called for to track

[1] Cruciform geometry enforces fracture to take place in the thinned center region of the sample, overriding local microstructural effects. The Marciniak test, on the other hand, creates a homogeneous multi-axially strained region where the fracture point is dictated by the microstructure.

plasticity and damage mechanisms along proportional and complex (non-proportional) biaxial strain paths, while employing various SEM mapping modes.

In this work, we present a novel approach that enables the use of SEM-based analytical techniques to study plasticity and damage mechanisms in samples deformed along proportional and complex biaxial strain paths. This was achieved by introducing a miniaturized bulge test setup with elliptical dies, featuring a sample holder adapted for EBSD/ECCI measurements and a method to impose strain path changes. This setup was employed in proof-of-principle experiments whereby thinned dual-phase steel samples and stainless steel foils were deformed at room temperature in biaxial strain paths while ECCI and EBSD were carried out incrementally to investigate microstructural mechanisms.

2. Methodology development

The bulge test is a method that can be used to measure biaxial stress-strain curves [46], parts of yield surfaces [47–50] and forming limit curves (FLC) [51], or characterize damage mechanisms [52] of sheet metal (as well as the mechanical response of thin films [53,54] or biological tissues [55,56]). Circular dies are typically used to investigate equi-biaxial strain paths, however elliptical dies can be employed to observe proportional strain paths with a strain ratio different from 1 [57–62]. Thanks to frictionless boundary conditions, simple analytical formulae can be used to assess the sample mechanical response. On top of these advantages, we demonstrate here that our hydraulic bulge test setup, with a dedicated sample holder, can also provide (i) non-proportional, complex, biaxial strain paths; and (ii) EBSD, ECCI and DIC measurements obtained in optimal experimental conditions. While the loading has to be carried out *ex situ*, the results presented here demonstrate that the test overcome most limitations found in interrupted tests, such as unloading or re-clamping effects.

2.1. Actuation, strain path control, multi-field mapping

In the developed method, a disc-shaped sample with a radius of 12mm and thickness of 100µm, is first clamped in a sample holder, then gradually pushed through an elliptical opening with hydraulic pressure (outside the SEM). As seen in ***Fig. 1****a*, the flat sample

deforms into a dome with a near elliptical shape. The pressure generator is set to deliver a linear increase in pressure with time, using ethanol as the hydraulic media. Ethanol was chosen as it doesn't contaminate the sample holder previous to SEM observations and avoid corrosion effects on the sample. For the proof-of-principle experiments, the lowest loading speed available was selected to perform quasi-static tests: for monotonic loadings, the maximum pressure available (230 bar) was reached in approximately 5 min. Initial strain rates at the center of the dome (as it is being formed) vary with both the thickness of each sample and the dies used but all values measured stayed below 10^{-3} s^{-1}. Note that the linear increase in pressure generates an exponential-like increase in strain rate as deformation proceeds. In our experiments, the highest strain rate measured before failure (with an acquisition rate of 1Hz) was $6.10^{-3}s^{-1}$.

The design of the sample holder ensures identical mechanical boundary conditions and consistent imaging conditions during the interrupted test. The holder can be taken to the SEM stage and back to the pressure chamber at any point during the experiment, without having to unclamp the sample being deformed. Several geometrical constraints have been considered during the design of the holder to be able to perform EBSD and ECCI in optimal conditions (e.g. 70° tilt, 15mm working distance for EBSD, and <10° tilt, 7mm working distance for ECCI). The sample holder can be placed on virtually any SEM stage (see *Fig. 2*) to carry out EBSD measurements at the center of the sample, in an optimal position. Conventional imaging (SE/BSE/In-lens) and ECCI observations are also conveniently performed because switching between different observation techniques is achieved by simply tilting the SEM stage.

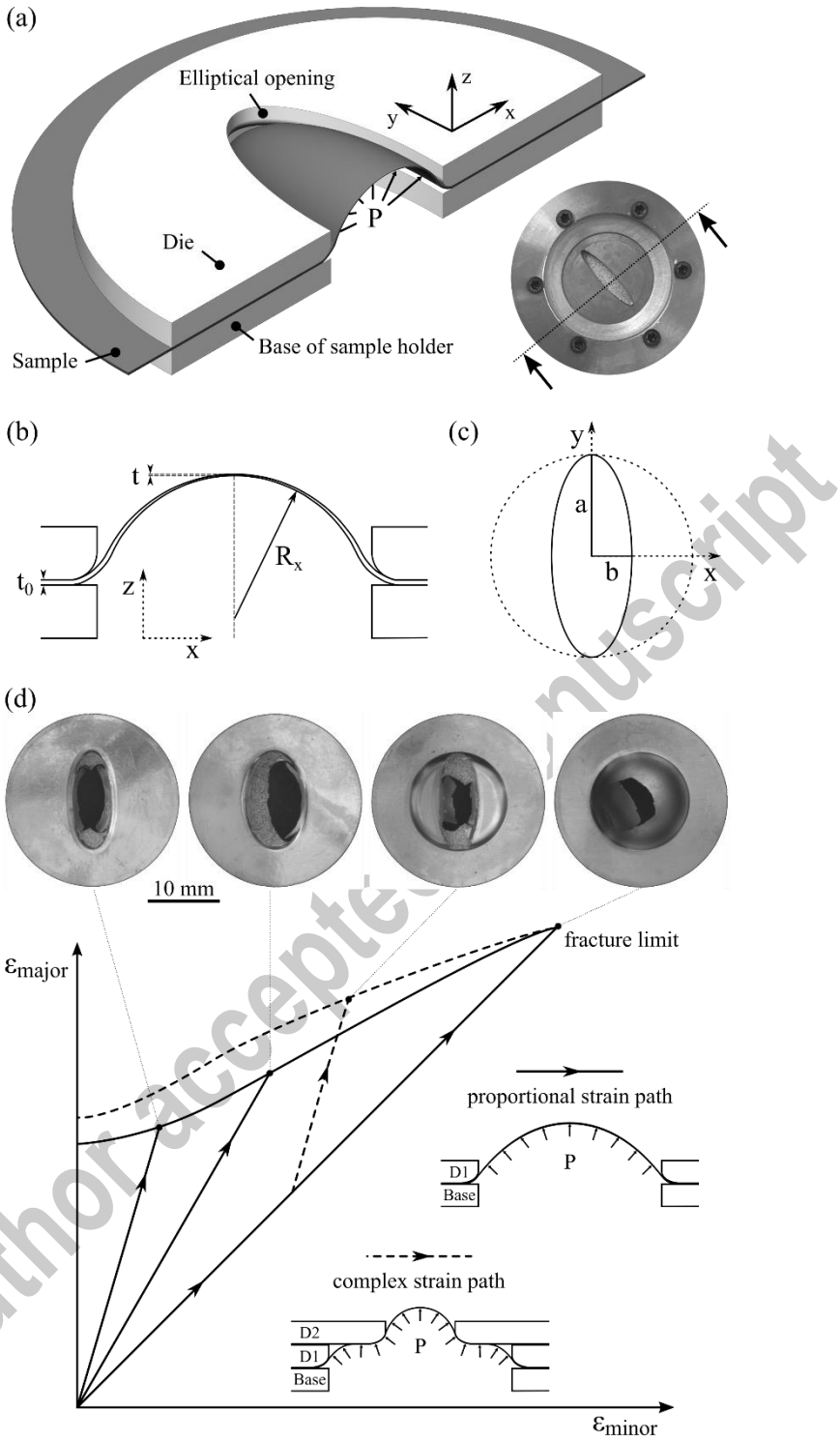

Fig. 1 Principle of a bulge test with elliptical dies. (a) Schematic view of the deformation experiment. A sample is clamped between the base of a custom sample holder and a die. Hydraulic pressure P is used to push the material through an elliptical opening in the die. The inset is a top view of the sample holder as fixed on the pressure generator during the test. (b) The thickness at the apex of the sample is denoted t and the initial thickness of the foil t_0. At the apex, $R = 1/c$ is the radius of curvature and c the local curvature of the surface. (c) Elliptical openings are characterized by their semi-major axis a and semi-minor axis b. (d) Illustration of biaxial strain paths achievable in a forming limit diagram of sheet metal. The top row shows optical images of stainless steel samples deformed to

failure with several elliptical openings. In the center of the sample, proportional strain paths are generated with a single die whereas complex strain paths are obtained with two overlapping dies.

The holder is composed primarily of a base in which the sample is positioned. On top it, one or two dies (1.04mm-thick) with elliptical openings are fitted and the holder is then sealed by applying a clamping force with a cover. The elliptical openings have a fixed semi-major axis of 6.5mm (denoted a in ***Fig. 1***c). Elliptical openings at the apex of the dome can be varied to impose strain paths ranging from equi-biaxial paths to plane strain [57–61]. Five dies have been manufactured with elliptical ratio b/a of 1, 0.8, 0.6, 0.4 and 0.2, where b is the semi-minor axis. All dies have a corner radius of 0.5mm to avoid stress concentration at the edge of the sample. To prevent draw-in, the dies are sand-blasted to obtain a rough (~10µm) surface. The quality of the clamping is evaluated after each test by comparing the external edge of the sample before and after the test using an optical camera. When a single die is used, a proportional stain path is obtained as illustrated in ***Fig. 1***d. When two overlapping dies with a decreasing b values are used, the sample undergoes a complex strain path: it deforms in the strain path associated with the first die until it reaches the second die which then changes the loading conditions towards a different strain path.

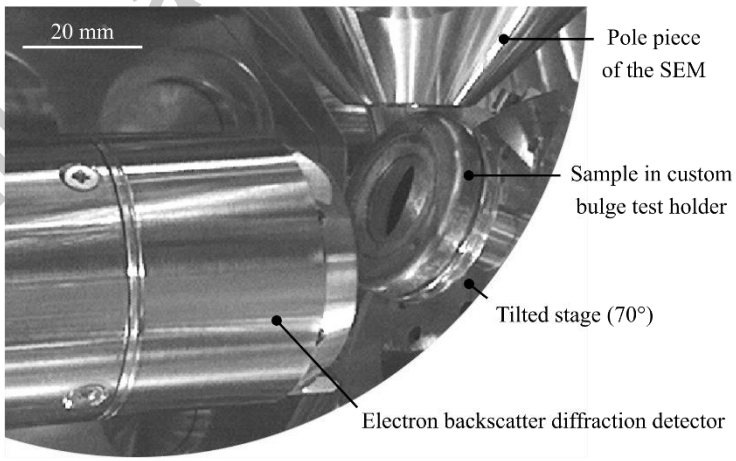

Fig. 2 Configuration used to perform EBSD acquisitions during interrupted bulge experiments (infrared image of the SEM chamber).

2.2. Shape, strain, stress measurements

Local shape and strain mapping are necessary to calculate the stress state at the apex of the bulged sample. We employed a stereovision optical system to perform strain mapping with the digital image correlation technique [46]. Such measurements could also be achieved by using SEM-based 3D DIC [63] while carefully considering artefacts such as SEM image distortions [64]. The stereovision system used to measure the bulge shape and surface strain fields was composed of two grey-scale digital cameras with a definition of 2452x2056 pixels and two 105mm AF Micro-Nikor lenses. The system was positioned vertically at a distance of 400mm (along the *z* axis in ***Fig. 1***), the distance between the two symmetrical cameras was 200mm and the angle between them 28°. In this configuration the field of view was roughly 18x15mm. An indirect homogenous lighting system was used to avoid glare on the sample surface. The aperture of the lenses was set to a f-value of 16 to observe the whole dome in focus with a high depth of field. The acquisition time was set to 40ms and the frame rate to 1Hz.

The software VIC-3D (Correlated Solutions) was used to acquire and process the data. To achieve a robust and accurate calibration, a miniaturized calibration object was manufactured on a flat glass slide by tapping a target printed on high density paper with a true black-and-white 1200 dpi printer. The calibration of the system was performed before each individual experiment to ensure that a calibration score smaller than 0.1pixel was met. Calibration was repeated each time to account for small movements of the cameras observed when the sample burst (no protection window was present between the sample and the lenses).

The correlation was carried out on 33x33pixel square subsets spaced out on a 10pixel grid. We used an eighth-order spline interpolation of gray levels and the displacement was calculated with a normalized correlation coefficient, searching for a homogeneous transformation. The logarithmic true strain field was calculated, using a smoothing filter of width 7. For stress-strain plots, the strain value reported is the mean strain in a disk of diameter 1mm around the apex of the dome. The apex is defined as the point of maximum displacement along the ***z*** axis

during the test (*cf.* ***Fig. 1***) and it is taken as the origin of the coordinate system on the initial configuration. The curvatures c_{xx} and c_{yy} at the apex (along the ellipse minor axis $\boldsymbol{x}$ and major axis $\boldsymbol{y}$) are estimated by fitting a quadratic surface to the current xyz data as described in the ISO standard [46]:

$$z(x,y) = a_0x^2 + a_1y^2 + a_2xy + a_3x + a_4y + a_5 \qquad (1)$$

The experimental xyz data considered for least-square minimization is extracted from an ellipse around the apex (with a semi major axis of 3mm and an elliptical ratio relevant to the die used). The a_i coefficients are then used to calculate the curvatures (neglecting non-vertical displacement of the apex) according to:

$$c_{xx} = \frac{2a_0}{(1+a_3^2)^{\frac{3}{2}}} \quad \text{and} \quad c_{yy} = \frac{2a_1}{(1+a_4^2)^{\frac{3}{2}}} \qquad (2)$$

The true thickness of the sample at the apex t is given by $t = t_0 \exp(\varepsilon_{zz})$ where t_0 is the initial thickness and ε_{zz} is the strain along the $\boldsymbol{z}$ direction. Considering plastic incompressibility and neglecting elastic strains, ε_{zz} is given with $\varepsilon_{zz} = -(\varepsilon_{xx} + \varepsilon_{yy})$. The thickness strain $\varepsilon_{thick} = -\varepsilon_{zz}$ was used to plot equi-biaxial stress-strain curves. The equivalent von Mises strain ε_{Mises} was used to detect patterns of localization in the strain field.

In bulge tests with elliptical dies, thin-membrane shell theory can only be applied to predict stresses if the sample surface forms an ellipsoid which is a shell of revolution. For simplicity, analytical formula using this hypothesis, established by Ragab and Habib [59] and discussed by Williams and Boyle [60] are considered here. At the apex where shear is negligible, the normal stress components are evaluated with:

$$\sigma_{xx} = \frac{P}{2\,t\,c_{xx}}\left(2 - \frac{c_{yy}}{c_{xx}}\right) \quad \text{and} \quad \sigma_{yy} = \frac{P}{2\,t\,c_{xx}} \qquad (3)$$

For circular dies, the biaxial stress σ_b is calculated as the equivalent von Mises stress:

$$\sigma_b = \sqrt{\frac{1}{2}\left(\sigma_{xx}^2 + \sigma_{yy}^2\right)} \qquad (4)$$

With circular dies, it is observed experimentally that $c_{xx} \approx c_{yy}$, therefore $\frac{c_{yy}}{c_{xx}} \approx 1$ and according to equation (3) $\sigma_{xx} \approx \sigma_{yy} \approx \frac{P}{2\,t\,c_{xx}}$. The standard relation for a thin spherical membrane in pure equi-biaxial stress state is met:

$$\sigma_b \approx \frac{PR}{2t} \quad \text{with} \quad \frac{1}{R} \approx c_{xx} \tag{5}$$

where R is the radius of curvature.

2.3. SEM-based observations

Samples prepared from DP600 steel were employed in two experiments to track microstructural evolutions with ECCI and EBSD. For both tests a single circular die was selected to generate equi-biaxial strain paths. In the first experiment, ECCI was performed with a Zeiss Merlin SEM operated at 20kV, with a beam intensity of 3nA. The surface of the sample was placed at a working distance of 7mm. Two successive observations were carried out at loading pressures of 0MPa and 9MPa. As describe above, the sample was clamped at the beginning of the experiment in the custom sample holder. It was first inserted in the SEM to take ECCI images and one EBSD map, then removed and loaded outside before being finally repositioned in the SEM for a second round of observations. To keep similar channeling conditions between the two ECCI images, care was taken (i) to place the sample holder twice in the same position on the SEM stage and (ii) to use small tilts and rotations (<5°) to compensate the rotation induced by the movement of the bulged surface, by matching several channeling contrasts in adjacent grains with the previous image. EBSD was performed with a step size of 50nm.

In the second experiment, 14 loading steps were investigated with SE and BSE images. Data was acquired with EBSD at the initial state (0 MPa), a loading pressure of 14MPa and 20MPa. A defect was introduced intentionally using a focused ion beam in a dual beam Helios 600 from FEI. The ion beam voltage was set at 30kV, a first cut was made with a beam intensity of 21nA and a depth of ~10µm then a second cut was performed on the edge of the first cut with a beam intensity of 2.8nA and a depth of ~3µm. The shape of the defect was chosen to be a star (with a diameter of 23µm) with the objective to localize stress on sharp points and

potentially initiate cracks. To reduce the cutting time, a pillar at the center of the star was kept intact. After the milling operation, the sample was repolished with OPS for 5 min to remove surface damage from FIB machining.

For SEM-based observations we used a Tescan Mira 3 equipped with a low-voltage YAG backscatter electron (BSE) detector and a Hikari Super EBSD detector from EDAX. The microscope was operated with a beam voltage of 30kV and a beam intensity of ~7nA (BI 19) in "depth" mode. For SE and BSE imaging, the sample was placed horizontally at a working distance of 15mm. For EBSD acquisitions, the sample was tilted 70° and placed at a working distance of 17mm. To make sure the observation area was correctly positioned in the chamber when working with EBSD on the elliptical surface, the following precautions were used: (i) the FIB defect was introduced at the center of the sample, close to the point where the surface stays parallel to the reference plane of the sample holder during the test. The uncertainty on the position of the defect was less than 1mm, a value that accounts for both the uncertainty on the position when milling the defect and the slack when placing the sample in the sample holder, (ii) the size of the area investigated was limited to 100µm, (iii) when placing the sample in EBSD position, the dynamic focus was first set to 70° then the sample tilt was adjusted to get a focused image of the area of interest. In this proof-of-principle experiment, image distortions and orientation errors arising from working on a curved surface were not compensated. The ability to get focused tilted images was taken as a safe sign to obtain EBSD maps with limited errors.

Three EBSD maps were acquired with a step size of 67nm and processed with the OIM Analysis software. Approximately 2% of the data was modified with a cleaning procedure using first a confidence index (CI) standardization filter and then a neighbor orientation correlation filter. Grain boundaries were defined with a 5° misorientation threshold. A kernel average misorientation (KAM) analysis was performed using kernels accounting for all points in the kernel up to second neighbors. Threshold values on the image quality (IQ) factor were used to discriminate martensite grains.

3. Proof-of-principle biaxial tests

In this part, we explore the range of proportional and complex biaxial strain paths that can be produced at the apex of samples deformed with the setup presented above. Strain and stress states at the apex of the bulge are the focus of the present study as this is the region where incremental EBSD observations can be carried out. Note that SEM imaging and ECCI can be conveniently used to track most parts of the sample. Samples of stainless steel foils and DP steel (prepared from bulk sheet metal) were tested. Stainless steel specimens were cut out of commercial foils, had a homogeneous thickness and homogeneous mechanical behaviors; therefore they made excellent validation samples. Commercial 316L stainless steel foils (Fe-16.8Cr-10.1Ni-2Mo-1.7Mn-0.02C wt%) provided by ATI Flat Rolled Products were cut out using wire EDM. A 78μm-thick foil was supplied in the annealed condition with a yield stress of 290MPa, a tensile strength of 660MPa and an elongation to failure greater than 60%. Two grades of DP steel were also employed in this study, with uniaxial tensile strength of approximately 600 MPa (DP600) and 800MPa (DP800). Both steel samples had to be prepared from bulk sheet metal following a procedure summarized in Appendix A.

A masking technique was developed to apply a DIC pattern exclusively at the center of the samples. The goal was to keep the clamped areas paint-free to avoid draw-in during the test. A laser cutter (Universal laser V-460) was used to cut and engrave commercial masking tape. Individual masks with an opening (matching the one in the die used later during the test) were manufactured and used to tape the samples on a flat aluminum sheet. The opening is precisely positioned at center of the sample using markings engraved in the tape. White paint was applied (SEM color coat #15603) and then a pattern of black ink (Super Black India ink) was deposited with an air brush. A pressure regulator was used to adjust the mean size of black dots (~10 pixels in the optical images used for DIC) and to get a flat white-to-black intensity distribution. The mask was removed easily by peeling it off thanks to the low adhesive power of the masking tape.

Twelve deformation experiments were carried out with stainless steel samples. In all of them, the foil transverse direction was aligned with the major axis of the elliptical opening. In the first ten experiments a single opening was used to produce proportional strain paths. Five elliptical ratios b/a (1, 0.8, 0.6, 0.4 and 0.2) were employed and each testing condition was repeated either twice (for elliptical ratios 0.8, 0.6, 0.4 and 0.2) or three times (for the circular case). In the last experiment, two overlapping openings with elliptical ratios 1 and 0.2 were used to generate a complex strain path. Four samples prepared from DP600 (two samples) and DP800 (two samples) were tested while an *in situ* DIC measurement was performed. A circular opening was employed to deform the two DP600 samples. Two overlapping openings with elliptical ratios 1 and 0.2 were employed with DP800 samples to generate complex strain paths.

3.1. Proportional strain paths

The range of strain paths produced in stainless steel and DP steel is shown in ***Fig. 3***. Five proportional strains paths were generated in stainless steel by using a single elliptical opening (***Fig. 3***a). Those paths were characterized by a principal strain ratio $\varepsilon_I/\varepsilon_{II}$ lying in the range 1 to 5 (see **Table** 1). For most paths, a non-linearity was observed as the deformation level increased: notably the equi-biaxial strain path deviates toward a strain ratio of 1.1 at 10% deformation where an ideal value of 1 was intuitively expected. This non-linearity is attributed to the anisotropic behavior of the foil associated with texture effects coming from the rolling processing steps, as well as to the requirement to reach plane strain condition, at necking. An excellent agreement was found between each pairs of repeated tests (characterized by a scatter in ε_{II} smaller than 0.2%) demonstrating the good repeatability of testing conditions. This agreement is also a direct consequence of the smooth nature of strain fields measured on the stainless steel samples as illustrated in ***Fig. 4*** and ***Fig. 5***. In ***Fig. 4***, three components of the strain field in a test performed with a 0.4 elliptical ratio are shown before failure. Even at high deformation levels (32%), normal strain components are localized at the center of the sample and shear deformation is strictly limited to the sides. Failed samples indicated cracking

patterns originating from the central part close to the bulge apex (see the failed samples used as illustrations in ***Fig. 1***).

Elliptical ratio b/a	1	0.8	0.6	0.4	0.2
Strain ratio $\varepsilon_I/\varepsilon_{II}$	1.1	1.4	1.7	2.4	5.0

Table 1 Principal strain ratio for stainless steel samples

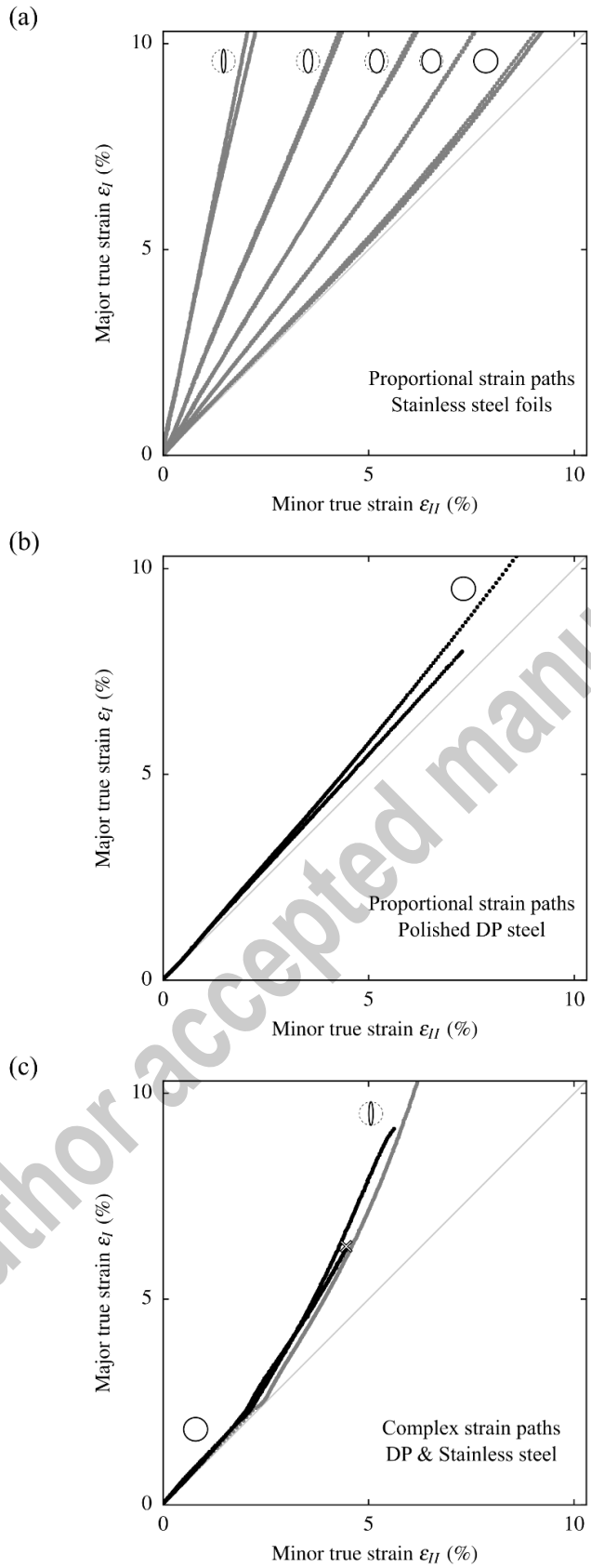

Fig. 3 Strain paths measured in stainless steel foils (grey) and polished DP steel samples (black). Failed samples are indicated by a cross and several tests were interrupted when reaching the maximum pressure available. (a) Proportional strain paths generated in homogeneous foils using single openings for five elliptical ratios b/a (0.2,

0.4, 0.6, 0.8 and 1). (b) Equi-biaxial stain paths obtained in thinned DP600 samples. (c) Complex strain paths obtained in stainless steel foils and thinned DP800 samples using two overlapping dies (elliptical ratios of 1 and 0.2). The cross indicates the failure of the sample.

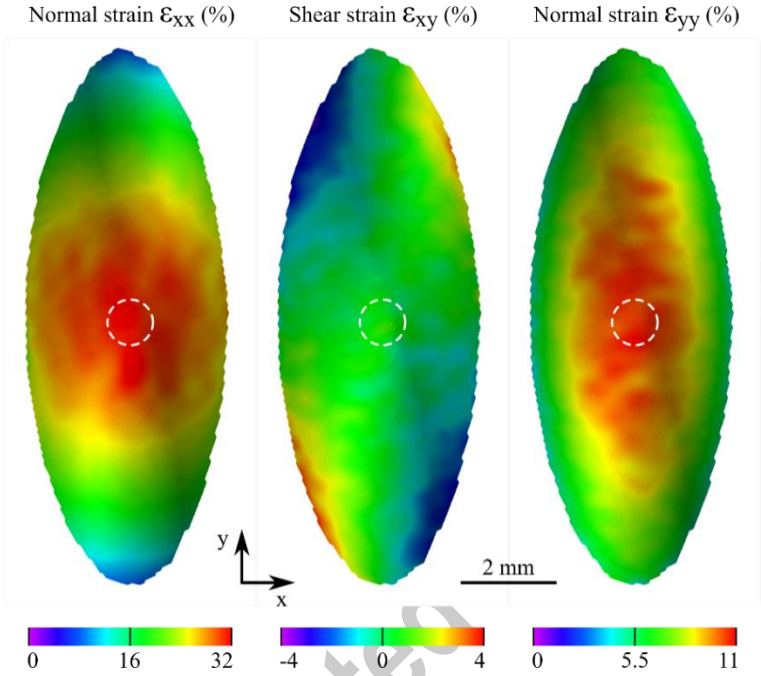

Fig. 4 : Strain field observed before failure in a stainless steel foil deformed through an opening with a 0.4 elliptical ratio. The white dashed line indicates the area of interest used to extract the strain path.

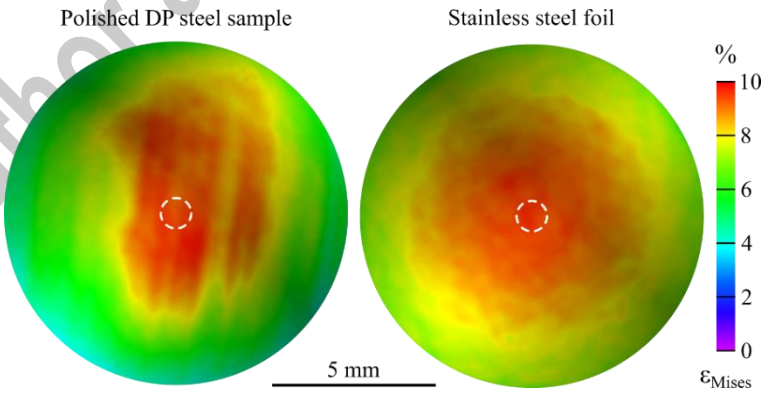

Fig. 5 Distribution of von Mises strain in a thinned DP steel sample (left) and a stainless steel foil (right). Both fields are shown for a major strain value ε_1 of 10% in the area of interest (dashed white circle). In stainless steel, a smooth strain field is observed localized around the apex of the bulge. In DP steel, strain localization is heterogeneous and occurs also away from the apex.

Proportional strain paths measured on DP600 samples with circular openings are presented in ***Fig. 3***b. The two paths have a strain ratio of 1.1 and 1.2 at 10% deformation respectively and are close to the strain paths observed in the stainless-steel foils. The non-linearity observed in this case is a consequence of heterogeneities in the strain field (see ***Fig. 5***), partly attributed to local variations of the sample thickness. Local thickness deviations in the bulged region can promote strain localization, also slightly thinner parts might not be clamped with the same efficiency as thicker parts. The two effects are mitigated by the high initial strain hardening of DP steel which encourages homogeneous plastic flow.

The equi-biaxial stress-strain curves associated with previous experiments are plotted in ***Fig. 6***. Only equi-biaxial curves are presented here for clarity but by using equations (3), the stress state can be estimated in non-proportional stain paths as well. Note that with elliptical openings the stress component σ_{yy} calculated from equation (3) tends to be underestimated (see [60]). In ***Fig. 6***, an abrupt elastic-plastic transition is observed around 300MPa in stainless steel followed by a linear hardening. For DP steel, continuous yielding is observed starting at 400MPa and rising up to approximately 5% deformation. For some curves, the elastic region is partially cut out and the stress-strain curve shifted towards lower strains because the thin samples are slightly pre-loaded before the acquisitions begin. This is the result of tightening the sample holder on the pressure chamber already filled with ethanol. For stainless steel with a homogeneous thickness, the scatter observed between the curves is of the order 10MPa. In the case of DP steel samples, a larger scatter (60MPa at 10% deformation) is seen, which may be arising from thickness variations among samples. Note that thickness influences several inputs used to evaluate the stress: the elliptical nature of the bulge shape, the strain state extracted at the apex and naturally the local thickness considered in the equation (5). For example, a 10% uncertainty on the local thickness will translate directly on a 10% uncertainty on the stress state calculated. Preparing samples with a homogeneous thickness is therefore a key aspect to successfully control both the strain path and stress state in the region of interest for later SEM observations (see Appendix A).

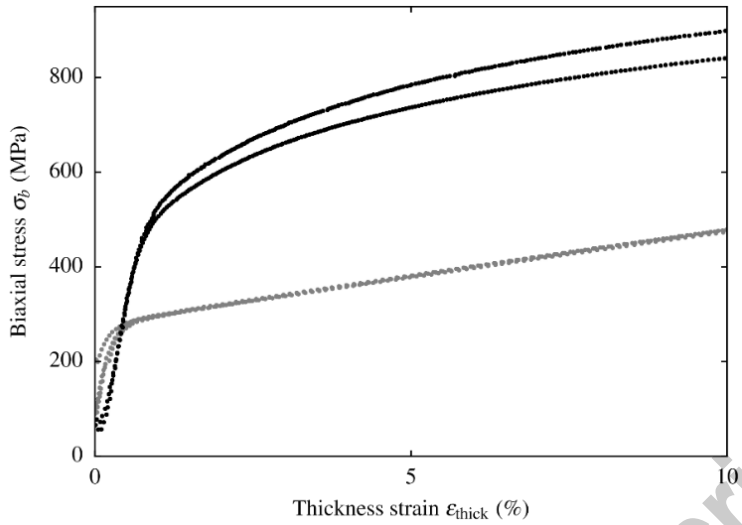

Fig. 6 Biaxial stress-strain curves measured in stainless steel foils (grey points) and DP600 steel samples (black points). Associated equi-biaxial strain paths are presented in **Fig. 3**a and **Fig. 3**b.

3.2. Complex strain paths

Complex strain paths obtained by using two overlapping openings with elliptical ratios 1 and 0.2 are presented in ***Fig. 3***c. In this case, the material first deforms along an equi-biaxial path up to 2.5% then switches towards a second path with a strain ratio of 2. The point of transition is fixed by the thickness of the first die and the size of the opening in second die. Both stainless steel and DP steel have been tested and the experimental data matches within 0.5%.

As illustrated in ***Fig. 7***, the generation of complex strain paths is a multi-step process which influences strain fields also far away for the central part of the sample. In a first step, the sample deforms freely following the path imposed by the first die as in previous proportional experiments. Then, the area around the bulge apex starts touching the lower surface of the second die. Because the pressure required to deform a sample through a small opening is high, the strain rate in the central part is significantly reduced while strain localization keeps building-up on the sides of the sample (underneath the second die and along the ellipse major axis). The sample spherical surface is therefore gradually pushed against the bottom side of the second die, letting the pressure increase in the chamber until the central part can flow in the second opening (third step). Despite this complex process, the central area of the sample undergoes a sharp strain path transition and no significant shearing is observed.

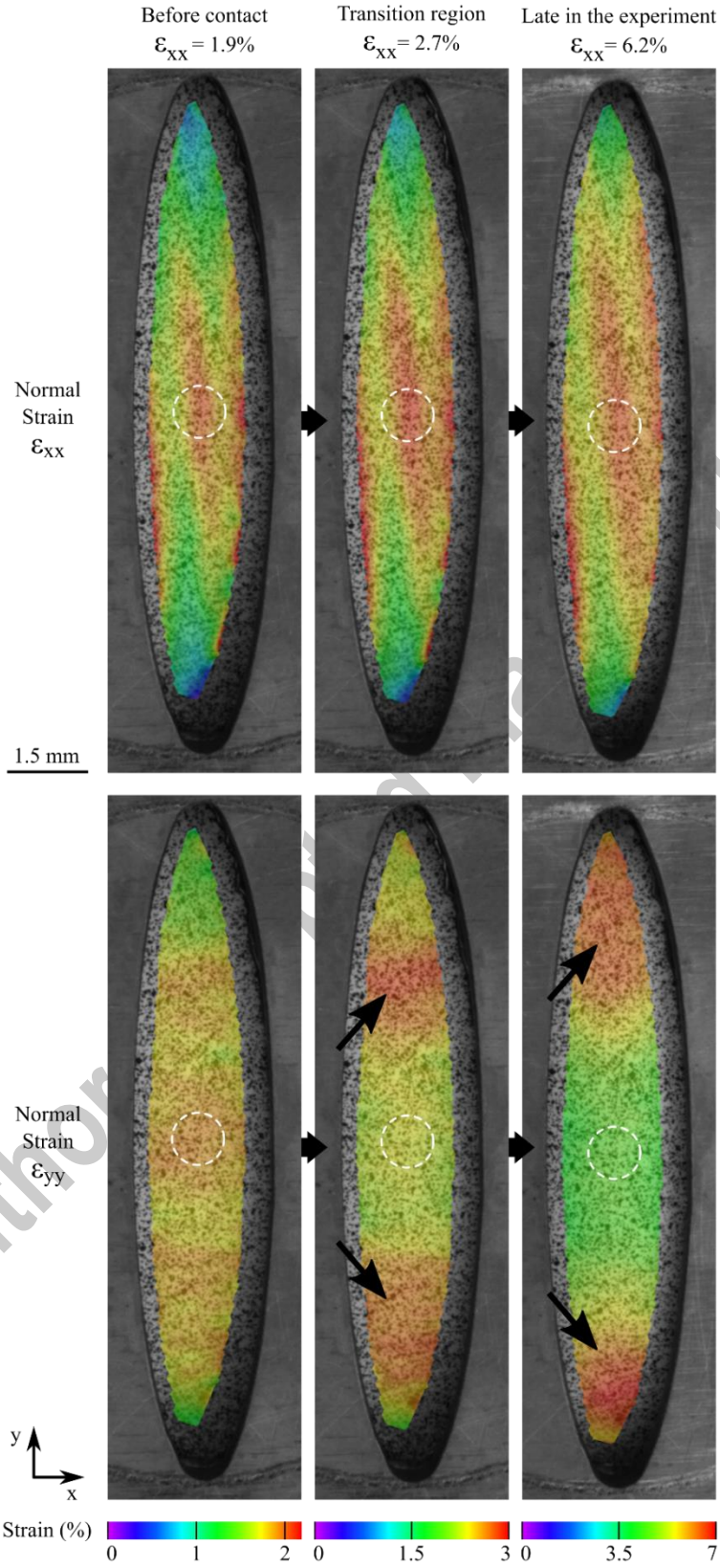

Fig. 7 Evolution of strain fields in DP800 steel deformed along a complex strain path. White dashed lines indicate the area used to extract the strain path reported in **Fig. 3**c. Black arrows point to strain localization happening below the second overlapping die. In the left column, the sample is still deforming along the equi-biaxial path imposed by

the first circular die. The mean intensity of the two components (ε_{xx} and ε_{yy}) is similar in the region of interest despite a limited localization observed on ε_{xx}. In the middle column, the central part of the sample has gotten in contact with the bottom around the opening of the second die. Significant strain localization is observed on ε_{yy} as the sample keeps deforming below the die. In the right column, the central part of the sample is now deforming along the strain path imposed by the second die. The strain localization pattern observed on ε_{yy} has intensified and moved further away from the center of the sample.

An important point to notice is that the strain ratio obtained with the second die, 2, is different from the strain ratio observed with the same die in a single proportional experiment, 5. This gap is explained by the difference in boundary conditions between the two tests: in the complex stain path experiment, the material is lightly flowing at the edge of the opening whereas it is fixed in the conventional test. Because the sample is maintained by the hydraulic pressure against the bottom side of the second die, complex strain paths are efficiently generated only when the difference in ellipse ratios between the first and second opening are high., i.e. with narrow second openings. In the current geometry of the sample holder, a strain ratio of 2 was the highest value obtained. The use of narrower openings to increase strain ratios would raise several experimental challenges such as the presence of bending strains, a need for higher pressure and a limited collection angle for EBSD and ECCI.

4. Case-studies involving ECCI and EBSD measurements

In this part, we show how incremental ECCI and EBSD observations during bulge experiments can provide valuable insights into the mechanisms of strain localization and damage nucleation in DP steels. Strain path effects have key impacts on damage events [2] and the formability of sheet metal [65,66]. In what follows, SEM-based techniques are used to provide quantitative and qualitative data on localized plasticity and damage at different length scale in the microstructure. Incremental ECCI is used to track dislocation activity at early stages of plasticity, in a configuration relevant to investigate mechanisms activated in the elasto-plastic transition or in fatigue loadings. EBSD-based quantitative analyses such as KAM approaches are then used to characterize strain localization around a defect in a configuration usually employed to study damage nucleation. In the literature, both techniques

(EBSD and ECCI) have been coupled recently on deformed samples to investigate the impact of grain and interphase boundaries on the triggering mechanisms of micro-damage features [27]. The bulge test method presented here opens the way for similar observations being performed at several deformation levels in biaxial loadings, along with local strain field measurements, for a better characterization of mechanical and microstructural effects on damage nucleation and growth.

4.1. Incremental observations

Fig. 8 shows the dislocation activity observed with incremental ECCI at low deformation in a large ferrite grain. The grain was positioned to obtain a uniform channeling contrast (dark). A region slightly misoriented in the grain (***Fig. 8***e), resulting in a white contrast, was chosen as the area of interest (***Fig. 8***b-c-d). In ***Fig. 8***b, a dense network of dislocations can be seen in the left part of this region. In the ferrite, fewer dislocations are observed especially towards the interior of the grain on the right side, as shown in ***Fig. 8***c. After 1.5-2% global strain, heterogeneous dislocation activity is observed (see ***Fig. 8***d). The dense dislocation sub-structure (i.e. the area shown with the black full ellipse) exhibits little movement as dislocations are likely to be pinned by each other. Clear dislocation slip is observed where the initial dislocation density was much lower (e.g. the area encircled with dashed lines).

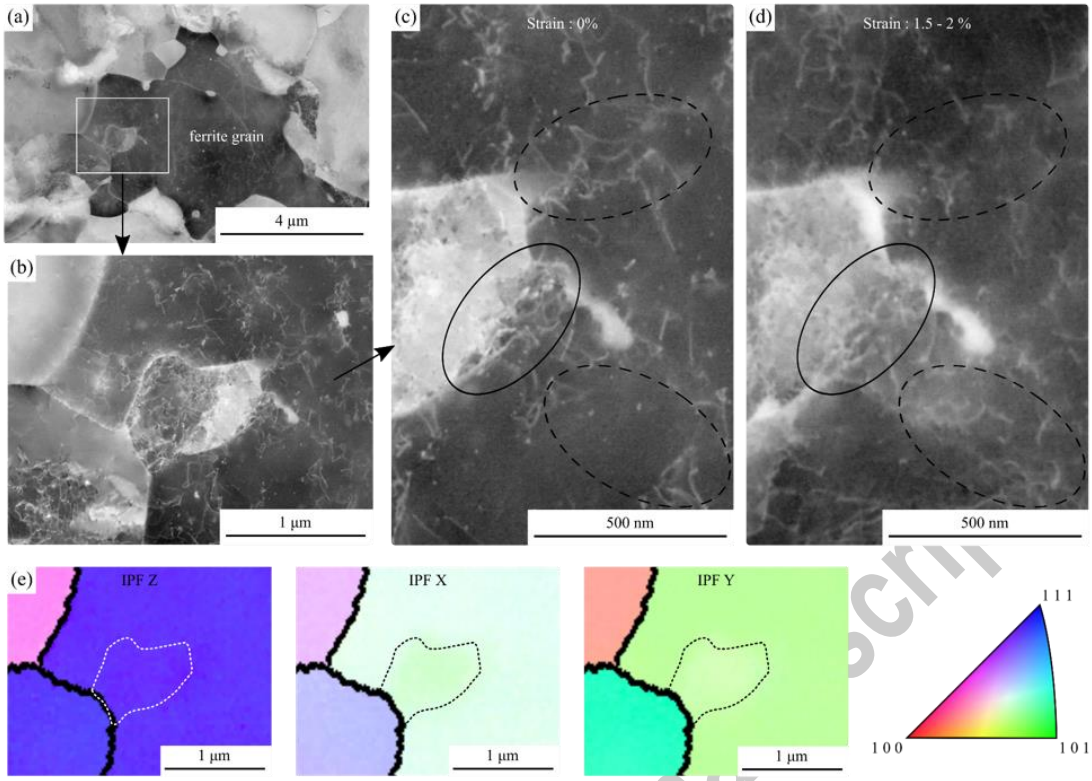

Fig. 8 Dislocation activity reveal by ECCI in a ferrite grain (DP steel loaded in biaxial tension). (a) Overview of the ferrite grain showing a dislocation sub-structure selected as region of interest. (b) A high defect density in observed in the substructure compared to the surroundings. The white homogeneous contrast reveals a slight misorientation with the parent grain. (c) and (d) Evolution of the dislocation network with the loading showing defects pinned close to the sub-structure (plain lines) and dislocation slip in the vicinity (dashed lines). (e) Inverse pole figure maps of the region of interest showing no significant misorientation between the sub-structure (indicated with dashed lines) and the parent grain

Fig. 9 shows how conventional EBSD can be used to characterize the evolution of strain localization and microstructure evolution around a sharp defect promoting stress concentration. As seen in the SEM images of ***Fig. 9***a, the star-shaped multi-notch defect (introduced by FIB in the microstructure) slightly opens-up as deformation proceeds. Surface roughening is observed above a loading pressure of 13MPa. As pointed out by white arrows, characteristic surface traces develop on the left side of the star, away from two of the sharp tips. A quantitative assessment of plastic deformation in the surrounding microstructure is presented in ***Fig. 9***b. The kernel average misorientation analysis demonstrates that local misorientations globally increase with the loading. This increase can be regarded as a marker of local plastic deformation which appears localized in the bottom-left and top-right parts of

the area investigated. In contrast, the top and bottom-right parts show fewer signs of plastic activity. Strain localization is notably observed in a 10µm-thick ring around the defect, with hot spots at the tips of the star. As seen in ***Fig. 10***a, steep increases in local misorientation are observed in regions with a high martensite content and small ferrite gain size. In region A, featuring ferrite grains with a size below 4µm, a first damage incident is observed with the shape of a micro-crack, for a loading pressure of 13MPa. At 17MPa, slight propagation of the first micro-crack is observed along with several other damage events occurring mostly at the boundary of two martensite islands. At 20MPa, a large crack is nucleated at the tip of the star in a ferrite grain, likely a result of local stress concentration due to a notch effect. In region B, two large ferrite grains (with a size greater than 4 µm) are investigated. In that region, far from grain boundaries, a slip band is developing from the star tip. Early signs of the band are detected at a loading pressure of 8MPa. A slip trace analysis using the orientation data confirmed that the band observed is consistent with slipping occurring in {110} crystal planes.

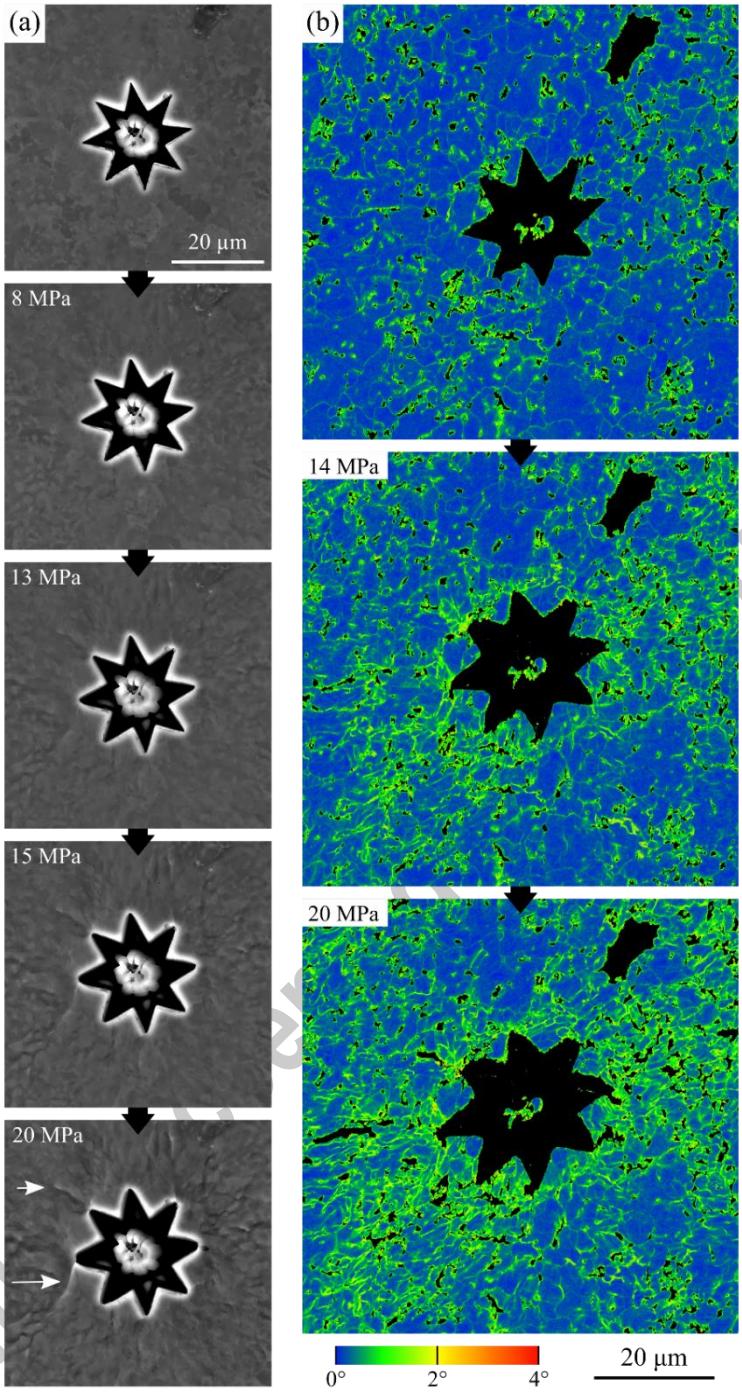

Fig. 9 Localized plasticity in the vicinity of an artificial defect revealed with SE images and KAM maps. (a) The defect is deformed in equi-biaxial tension as the loading pressure increases. White arrows indicate slip bands developing from the sharp tips of the star. (b) KAM maps show the evolution of local misorientations in the microstructure as plastic strains increase.

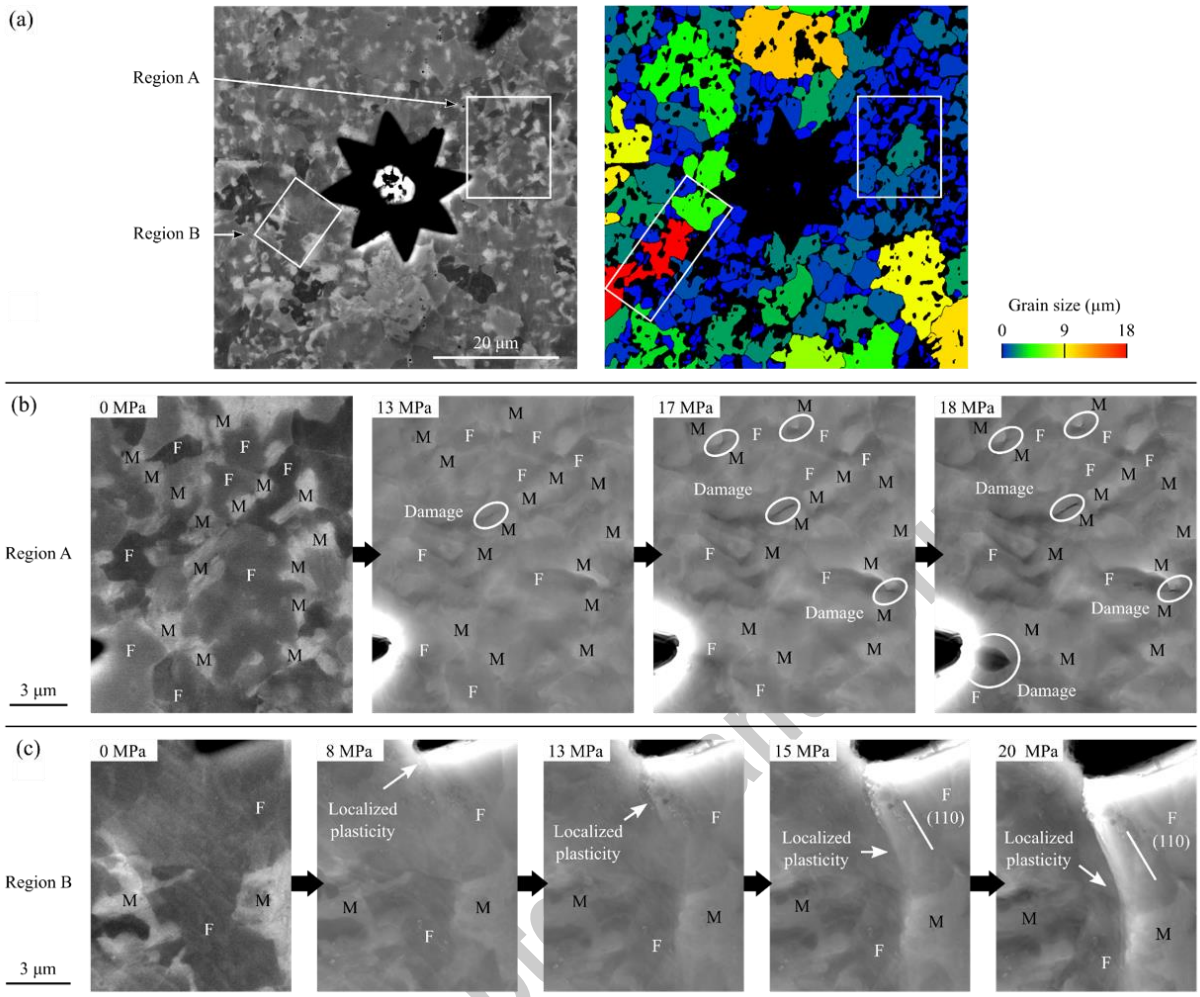

Fig. 10 Plasticity and damage mechanisms investigated around the defect presented in **Fig. 9**. (a) Two regions of interest are observed. As shown in the grain size map on the right, Region A features small ferrite grains and a high martensite content whereas Region B contains large ferrite grains. In Region A damage mechanisms are activated early (b) whereas localized slip is seen in the large ferrite grains of Region B (c).

4.2. Perspectives

The ability to track dislocations in biaxial strain paths with incremental ECCI opens up new perspectives for example regarding the investigation of continuous yielding. Dislocation slip at early deformation levels can be evaluated in specific locations such as the vicinity of martensite islands by selecting them using the large field of view of the SEM. In this manner, dislocation activity might be correlated to intragranular elastic strain stemming from the martensitic phase transformation by using an initial high angular resolution EBSD measurement on the flat sample. ECCI under controlled channeling conditions could certainly

be performed with the current setup by using an EBSD orientation measurement to control channeling conditions [20].

The ability to perform incremental EBSD with the bulge test approach, in a convenient manner, gives access to a quantitative evaluation of microstructural evolutions otherwise difficult to obtain in biaxial strain paths. As seen in ***Fig. 9*** and ***Fig. 10***, orientation imaging can provide valuable data on the role of microstructural features (slip systems activated, type of boundaries, etc.) and quantitative indices on some mechanical fields (plastic strains, GNDs, etc.) that could be correlated, for example, to damage initiation mechanisms [27]. One current limitation to the use of EBSD on bulged samples is the curvature of the surface, as current setups only feature scanning strategies adapted for flat surfaces. Additional orientation errors and image distortions are expected to arise because of an erroneous evaluation of the source point position on a curved surface. A detailed explanation of the impact of image distortions in conventional EBSD can be found in [67] and it should be noted that the determination of source point positions is a critical aspect of high angular resolution EBSD (see e.g. [68,69]). In the present experiment, a sharp tilted image of the small area of interest was obtained and it was assumed that the local misalignment of the surface was within the range typically observed when fixing samples onto an SEM stage.

As seen with these proof-of-concept experiments, a key benefit of SEM-based observations with the bulge test approach is to enable multi-scale measurements to be performed down to the dislocation scale. Our method is therefore expected to provide insights into the evolutions of spatially-resolved microstructural data, such as the distribution of phases and crystal orientations, that would be valuable, for example, for the investigation of deformation-induced phase transformations in TRIP steel [16,70]. Such datasets would also help calibrate crystal plasticity models through direct comparisons with full-field simulations [71]. The interrupted nature of the test is considered a limited drawback in most experiments where plastic deformation mechanisms are of interest: the analytical techniques considered here are time-consuming so even true *in situ* deformation experiments must be interrupted to perform the

measurements, allowing relaxation processes to occur. Thanks to the versatility of the sample holder, the full potential of the method lies in the ability to couple measurements from multiple techniques (e.g. DIC and EBSD [72]), at each loading step, to investigate mechanisms activated in biaxial loadings along proportional and complex strain paths.

5. Summary Remarks and Conclusion

A method has been developed to track site-specific microstructure evolutions and local mechanical fields in metallic samples deformed along biaxial strain paths. The method is based on interrupted bulge tests carried out with a custom sample holder adapted for SEM-based analytical measurements. Elliptical dies have been used to generate proportional and complex strain paths in both commercial stainless steel foils and DP steel samples prepared from bulk sheet metal. With the current setup, proportional strain paths can be obtained with a strain ratio in the range 1 to 5 whereas complex strain paths are accessible with a secondary strain ratio of 2. With two proof-of-concept experiments, it has been demonstrated that incremental EBSD and ECCI can be conducted conveniently in configurations relevant for multi-scale investigations of localized plasticity and damage mechanisms in DP steel. The versatility of the method enables the characterization of fundamental mechanisms of plasticity and damage activated in proportional and complex biaxial loadings.

6. Acknowledgements

We gratefully acknowledge Michael J. Tarkanian, James Hunter, David Bono, Qilong Cheng and Jiyun Kang for their input in the design of the bulge test setup. Valuable help provided by Ashley Brown Raynal is gratefully acknowledged. The authors thank Pr. Tomasz Wierzbicki and Pr. Ian Hunter for their kindly support. Dr. Guilhem Martin is acknowledged for his assistance in the finalization of this manuscript. This work made use of the shared experimental facilities supported in part by the MRSEC program of the National Science Foundation under award number DMR – 1419807.

7. Appendix A: Development of a thinning process for DP Steel

DP600 and DP800 steel used in this study were non-commercial grades provided by Tata Steel (IJmuiden, the Netherlands) in the shape of 1.3mm-thick sheets. The following thinning method was developed to prepare thin samples from the thick commercial sheets. The goal was to obtain EBSD-polished samples with a homogeneous thickness (typically 100µm $\pm$5 µm) to perform well-controlled bulge tests. The composition and overall properties of these two steels are provided in Table 2 for reference.

Steel	C (%wt)	Mn (%wt)	Si (wt%)	Martensite (%)	Ferrite grain size (µm)	Martensite grain size (µm)
DP600	0.09	1.68	0.24	17.2	8.4±6.1	2.7±1.6
DP800	0.15	1.71	0.25	18.4	4.9±1.9	1.7±1.1

Table 2 Characteristics of the DP steel used in this work

The first preparation step (illustrated in ***Fig. 11***a) consisted in cutting a 300µm-thick sample out of the 1.3mm-thick sheet using a wire EDM machine (Charmilles Robofil 1020SI). To perform a homogeneous cut, the sheet was clamped in a precision tool maker vise on both sides. Then, a disk of diameter 24mm was cut out with the same process. As schematized in ***Fig. 11***b, the cutting introduces damaged layers on both surfaces which had to be removed by polishing. These layers bear compressive residual stress and make the polishing step a complex task as samples progressively bend when the damaged layer is removed from one side. A cross section observation of the damaged layer was performed to estimate its depth below 60µm (cf. ***Fig. 11***c). As a safe target, 100µm of mater was removed on both sides, by polishing, to obtain a sample with a microstructure fully representative of the original one.

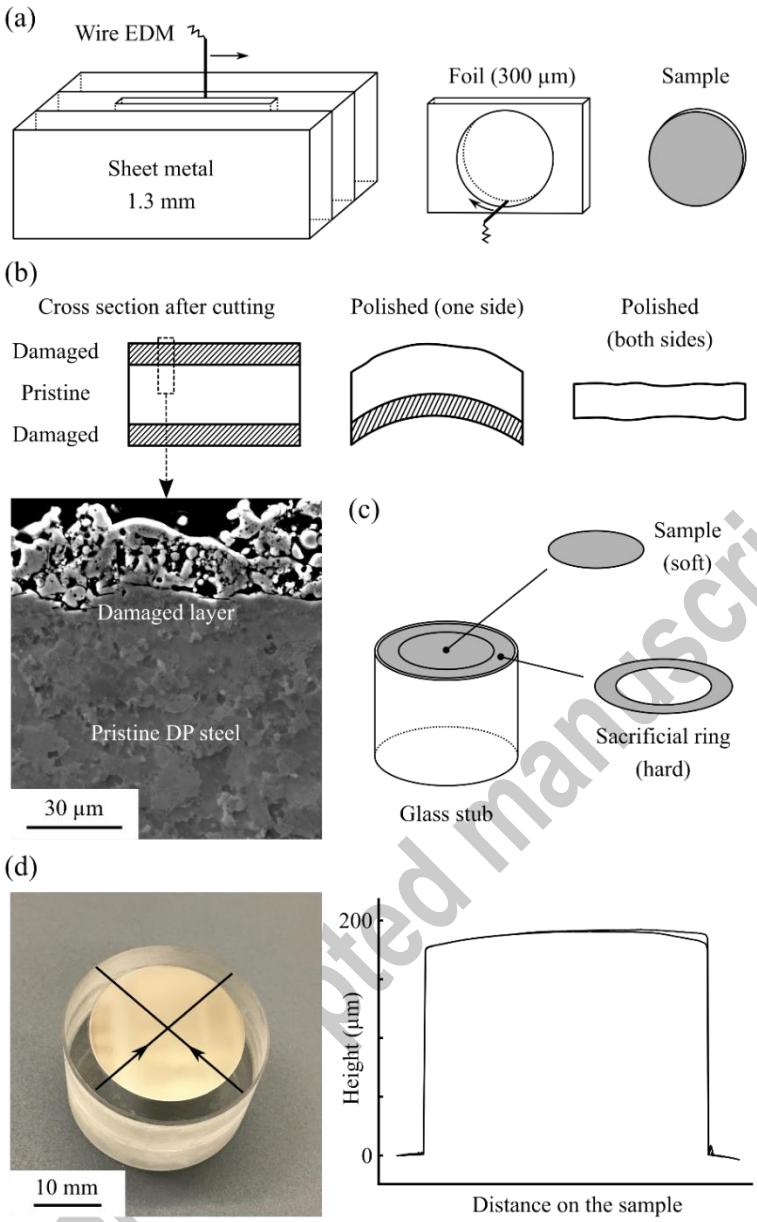

Fig. 11 Overview of the thinning process used to prepare polished samples from DP steel sheets. (a) Wire electrical discharge machining is used to extract 300µm-thick disks from commercial sheet metal. (b) Schematic view of a disk cross-section at different stages of polishing. Damaged surface layers inherited from the cutting step are present initially as shown in inset (SE image). Thickness inhomogeneity and slight shape waviness results from the two-step polishing process. (c) Illustration of the experimental configuration used for automated polishing. (d) Profilometery measurements used to check the performance of the gluing process. The optical image shows a sample glued on a glass stub and polished on one side. Sacrificial rings were not used here to keep the glass surface as a reference. The profile measurements shown on the right were carried out along the two black lines.

The following procedure gave the best results for polishing the sample while keeping a homogeneous thickness. First, sacrificial rings were cut out using a waterjet cutter from hardened stainless steel foils (yield strength of 1240MPa). When the first side of the sample

was polished, a 200µm-thick foil was used whereas a 100µm-thick one was used for the second side. One sacrificial ring was fixed with super glue on a borosilicate glass stub (McMaster-Carr) fitting in an automated polisher (*cf.* ***Fig. 11***c). The surface of the glass stub was extremely flat, within ±1µm (measurement realized with a stylus profilometer DekTakTX from Bruker). To glue the ring, the stub was positioned in a vertical precision vise, the glue was deposited, and then the ring, a foil of Teflon and finally a second glass stub before closing the vise. The Teflon foil keeps the glue from adhering on the second glass stub and can simply be removed by peeling it off. The sample was then glued in the center of the ring with the same procedure. The quality of the gluing was checked by looking at the transparent backside of the stub. Three glass stubs were inserted in an automated polishing machine (to maintain balance and avoid wobbling movements) and they were polished with a 9µm diamond solution on a hard polishing cloth. The polishing step was stopped when the sacrificial ring (originally thinner than the sample) started to get polished on the whole surface. Conventional polishing steps were then used to reach a 1µm polishing grade (first side) or a OPS polishing grade (second side). Three baths of acetone were used to unglue and clean the samples.

One difficulty we faced was to monitor the sample thicknesses as the thinning process introduces a slight waviness in their shape. This waviness is likely caused by released residual stress initially present in the rolled thick sheet. The challenge with profilometery techniques was to hold and flatten the sample properly (with glue or a magnet) and still get an absolute measurement of the thickness. In further experiments, one should consider using X-ray tomography to get a 3D visualization of the sample and hence decouple shape waviness from thickness variations. A mechanical profilometer (DekTakTX, Bruker) was used several times to make sure the top surface after gluing was parallel to the glass stub (cf. ***Fig. 11***d). However, because of the variability in the layer of glue deposited, an estimation of the absolute thickness by this method was hardly reliable. As a consequence, the thicknesses reported in Table 3 have been measured simply with a caliper at four points on the sample. For DP600 samples, polished without using sacrificial polishing rings but with a similar process, the scatter found

was in the order of 10μm. For DP800, the scatter found was in the order of 5μm. This decreased in scatter is attributed to the stability and corrective mechanism provided by the sacrificial rings. Note that when only the central part of the sample is considered (the tested area), the thickness scatter reported in Table 3 can be considered an upper bound.

Sample name	DP600 DIC_1	DP600 DIC_2	DP800 DIC_3*	DP800 DIC_4*	DP600 ECCI_1*	DP600 EBSD_1
Thickness (μm))	148 ±10	143 ±13	60 ±6	87 ±4	145 ±6	110 ±11

Table 3 Sample thicknesses evaluated after polishing. The star symbol indicates samples polished with a sacrificial ring following the procedure detailed above.

8. References

[1] C.C. Tasan, J.P.M. Hoefnagels, C.H.L.J. ten Horn, M.G.D. Geers, Experimental analysis of strain path dependent ductile damage mechanics and forming limits, Mech. Mater. 41 (2009) 1264–1276. doi:10.1016/j.mechmat.2009.08.003.

[2] J.P.M. Hoefnagels, C.C. Tasan, F. Maresca, F.J. Peters, V.G. Kouznetsova, Retardation of plastic instability via damage-enabled microstrain delocalization, J. Mater. Sci. 50 (2015) 6882–6897. doi:10.1007/s10853-015-9164-0.

[3] M.F. Horstemeyer, J. Lathrop, A.M. Gokhale, M. Dighe, Modeling stress state dependent damage evolution in a cast Al-Si-Mg aluminum alloy, Theor. Appl. Fract. Mech. 33 (2000) 31–47. doi:https://doi.org/10.1016/S0167-8442(99)00049-X.

[4] N. Bonora, D. Gentile, A. Pirondi, G. Newaz, Ductile damage evolution under triaxial state of stress: Theory and experiments, Int. J. Plast. 21 (2005) 981–1007. doi:10.1016/j.ijplas.2004.06.003.

[5] L. Xue, Damage accumulation and fracture initiation in uncracked ductile solids subject to triaxial loading, Int. J. Solids Struct. 44 (2007) 5163–5181. doi:10.1016/j.ijsolstr.2006.12.026.

[6] B. Gardey, S. Bouvier, V. Richard, B. Bacroix, Texture and dislocation structures observation in a dual-phase steel under strain-path changes at large deformation, Mater. Sci. Eng. A. 400–401 (2005) 136–141. doi:10.1016/j.msea.2005.01.066.

[7] I.A. Volkov, Y.G. Korotkikh, I.S. Tarasov, Modeling complex plastic deformation and fracture of metals under disproportionate loading, J. Appl. Mech. Tech. Phys. 50 (2009) 891–900.

[8] R. Lapovok, D. Hodgson, A damage accumulation model for complex strain paths: Prediction of ductile failure in metals, J. Mech. Phys. Solids. 57 (2009) 1851–1864. doi:10.1016/j.jmps.2009.07.008.

[9] L. Dietrich, G. Socha, Accumulation of damage in A336 GR5 structural steel subject to complex stress loading, Strain. 48 (2012) 279–285. doi:10.1111/j.1475-1305.2011.00821.x.

[10] J. Kang, Y. Ososkov, J.D. Embury, D.S. Wilkinson, Digital image correlation studies for microscopic strain distribution and damage in dual phase steels, Scr. Mater. 56 (2007) 999–1002. doi:10.1016/j.scriptamat.2007.01.031.

[11] C.C. Tasan, M. Diehl, D. Yan, C. Zambaldi, P. Shanthraj, F. Roters, D. Raabe, Integrated experimental–simulation analysis of stress and strain partitioning in multiphase alloys, Acta Mater. 81 (2014) 386–400. doi:10.1016/j.actamat.2014.07.071.

[12] Q.G. Wang, Microstructural effects on the tensile and fracture behavior of aluminum casting alloys A356/357, Metall. Mater. Trans. A Phys. Metall. Mater. Sci. 34 (2003) 2887–2899. doi:10.1007/s11661-003-0189-7.

[13] T.R. Bieler, P. Eisenlohr, F. Roters, D. Kumar, D.E. Mason, M.A. Crimp, D. Raabe, The role of heterogeneous deformation on damage nucleation at grain boundaries in single phase metals, Int. J. Plast. 25 (2009) 1655–1683. doi:10.1016/j.ijplas.2008.09.002.

[14] A. Pineau, Development of the local approach to fracture over the past 25 years: Theory and applications, Int. J. Fract. 138 (2006) 139–166. doi:10.1007/s10704-006-0035-1.

[15] H. Li, M.W. Fu, J. Lu, H. Yang, Ductile fracture: Experiments and computations, Int. J. Plast. 27 (2011) 147–180. doi:10.1016/j.ijplas.2010.04.001.

[16] W. Wu, Y.W. Wang, P. Makrygiannis, F. Zhu, G.A. Thomas, L.G. Hector, X. Hu, X. Sun, Y. Ren, Deformation mode and strain path dependence of martensite phase transformation in a medium manganese TRIP steel, Mater. Sci. Eng. A. 711 (2018) 611–623. doi:10.1016/j.msea.2017.11.008.

[17] S.T. Oh, K.K. Park, H.N. Han, S.H. Park, K.H. Oh, Transformation Behavior of Retained Austenite in Hydroformed TRIP Steel, Mater. Sci. Forum. 408–412 (2009) 1341–1346. doi:10.4028/www.scientific.net/msf.408-412.1341.

[18] T. Iwamoto, T. Tsuta, Y. Tomita, Investigation on deformation mode dependence of strain-induced martensitic transformation in trip steels and modelling of transformation kinetics, Int. J. Mech. Sci. 40 (1998) 173–182. doi:10.1016/S0020-7403(97)00047-7.

[19] A.J. Schwartz, M. Kumar, B.L. Adams, D.P. Field, Electron Backscatter Diffraction in Materials Science, 2nd ed., Springer US, Boston, MA, 2009. doi:10.1007/978-0-387-88136-2.

[20] S. Zaefferer, N.N. Elhami, Theory and application of electron channelling contrast imaging under controlled diffraction conditions, Acta Mater. 75 (2014) 20–50. doi:10.1016/j.actamat.2014.04.018.

[21] F. Ram, Z. Li, S. Zaefferer, S.M. Hafez Haghighat, Z. Zhu, D. Raabe, R.C. Reed, On the origin of creep dislocations in a Ni-base, single-crystal superalloy: An ECCI, EBSD, and dislocation dynamics-based study, Acta Mater. 109 (2016) 151–161. doi:10.1016/j.actamat.2016.02.038.

[22] M. Kamaya, A.J. Wilkinson, J.M. Titchmarsh, Measurement of plastic strain of polycrystalline material by electron backscatter diffraction, Nucl. Eng. Des. 235 (2005) 713–725. doi:10.1016/j.nucengdes.2004.11.006.

[23] W. Pantleon, Resolving the geometrically necessary dislocation content by conventional electron backscattering diffraction, Scr. Mater. 58 (2008) 994–997. doi:10.1016/j.scriptamat.2008.01.050.

[24] A.J. Wilkinson, G. Meaden, D.J. Dingley, High-resolution elastic strain measurement from electron backscatter diffraction patterns: New levels of sensitivity, Ultramicroscopy. 106 (2006) 307–313. doi:10.1016/j.ultramic.2005.10.001.

[25] C. Maurice, J.H. Driver, R. Fortunier, On solving the orientation gradient dependency of high angular resolution EBSD, Ultramicroscopy. 113 (2012) 171–181. doi:10.1016/j.ultramic.2011.10.013.

[26] E. Plancher, J. Petit, C. Maurice, V. Favier, L. Saintoyant, D. Loisnard, N. Rupin, J.B.

Marijon, O. Ulrich, M. Bornert, J.S. Micha, O. Robach, O. Castelnau, On the Accuracy of Elastic Strain Field Measurements by Laue Microdiffraction and High-Resolution EBSD: a Cross-Validation Experiment, Exp. Mech. 56 (2016) 483–492. doi:10.1007/s11340-015-0114-1.

[27] F. Archie, X. Li, S. Zaefferer, Micro-damage initiation in ferrite-martensite DP microstructures: A statistical characterization of crystallographic and chemical parameters, Mater. Sci. Eng. A. 701 (2017) 302–313. doi:10.1016/j.msea.2017.06.094.

[28] C. Caër, R. Pesci, Local behavior of an AISI 304 stainless steel submitted to in situ biaxial loading in SEM, Mater. Sci. Eng. A. 690 (2017) 44–51. doi:10.1016/j.msea.2017.02.087.

[29] M.A. Sutton, J.-J. Orteu, H.W. Schreier, Image Correlation for Shape, Motion and Deformation Measurements, 2009. doi:10.1017/CBO9781107415324.004.

[30] M.A. Sutton, N. Li, D.C. Joy, A.P. Reynolds, X. Li, Scanning electron microscopy for quantitative small and large deformation measurements Part I: SEM imaging at magnifications from 200 to 10,000, Exp. Mech. 47 (2007) 775–787. doi:10.1007/s11340-007-9042-z.

[31] L. Allais, M. Bornert, T. Bretheau, D. Caldemaison, Experimental characterization of the local strain field in a heterogeneous elastoplastic material, Acta Metall. Mater. 42 (1994) 3865–3880.

[32] D. Yan, C.C. Tasan, D. Raabe, High resolution in situ mapping of microstrain and microstructure evolution reveals damage resistance criteria in dual phase steels, Acta Mater. 96 (2015) 399–409. doi:10.1016/j.actamat.2015.05.038.

[33] D. Fullwood, M. Vaudin, C. Daniels, T. Ruggles, S.I. Wright, Validation of kinematically simulated pattern HR-EBSD for measuring absolute strains and lattice tetragonality, Mater. Charact. 107 (2015) 270–277. doi:10.1016/j.matchar.2015.07.017.

[34] T. Vermeij, M. De Graef, J. Hoefnagels, Demonstrating the potential of accurate absolute cross-grain stress and orientation correlation using electron backscatter diffraction, Scr. Mater. 162 (2019) 266–271. doi:10.1016/j.scriptamat.2018.11.030.

[35] E. Plancher, V. Favier, C. Maurice, E. Bosso, N. Rupin, J. Stodolna, D. Loisnard, J.B. Marijon, J. Petit, J.S. Micha, O. Robach, O. Castelnau, Direct measurement of local constitutive relations, at the micrometre scale, in bulk metallic alloys, J. Appl. Crystallogr. 50 (2017) 1–9. doi:10.1107/S1600576717006185.

[36] A. Tatschl, O. Kolednik, On the experimental characterization of crystal plasticity in polycrystals, Mater. Sci. Eng. A. 342 (2003) 152–168. doi:10.1016/S0921-5093(02)00278-2.

[37] C.C. Tasan, M. Diehl, D. Yan, C. Zambaldi, P. Shanthraj, F. Roters, D. Raabe, Integrated experimental-simulation analysis of stress and strain partitioning in multiphase alloys, Acta Mater. 81 (2014) 386–400. doi:10.1016/j.actamat.2014.07.071.

[38] E.A. Torres, A.J. Ramírez, *In situ* scanning electron microscopy, Sci. Technol. Weld. Join. 16 (2011) 68–78. doi:10.1179/136217110X12785889550028.

[39] H. Ghadbeigi, C. Pinna, S. Celotto, Failure mechanisms in DP600 steel: Initiation, evolution and fracture, Mater. Sci. Eng. A. 588 (2013) 420–431. doi:10.1016/j.msea.2013.09.048.

[40] A. Alaie, S. Ziaei Rad, J. Kadkhodapour, M. Jafari, M. Asadi Asadabad, S. Schmauder, Effect of microstructure pattern on the strain localization in DP600 steels analyzed using combined in-situ experimental test and numerical simulation, Mater. Sci. Eng. A. 638 (2015) 251–261. doi:10.1016/j.msea.2015.04.071.

[41] C.C. Tasan, J.P.M. Hoefnagels, M.G.D. Geers, Microstructural banding effects

clarified through micrographic digital image correlation, Scr. Mater. 62 (2010) 835–838. doi:10.1016/j.scriptamat.2010.02.014.

[42] C.C. Tasan, J.P.M. Hoefnagels, E.C.A. Dekkers, M.G.D. Geers, Multi-Axial Deformation Setup for Microscopic Testing of Sheet Metal to Fracture, Exp. Mech. 52 (2012) 669–678. doi:10.1007/s11340-011-9532-x.

[43] S. Van Petegem, A. Guitton, M. Dupraz, A. Bollhalder, K. Sofinowski, M. V. Upadhyay, H. Van Swygenhoven, A Miniaturized Biaxial Deformation Rig for in Situ Mechanical Testing, Exp. Mech. 57 (2017) 569–580. doi:10.1007/s11340-016-0244-0.

[44] M.B. Gorji, D. Mohr, Micro-tension and micro-shear experiments to characterize stress-state dependent ductile fracture, Acta Mater. 131 (2017) 65–76. doi:10.1016/j.actamat.2017.03.034.

[45] M. Kubo, H. Yoshida, A. Uenishi, S. Suzuki, Y. Nakazawa, Development of Biaxial Tensile Test System for In-situ Scanning Electron Microscope and Electron Backscatter Diffraction Analysis, 56 (2016) 669–677.

[46] ISO 16808, ISO 16808:2014 Metallic materials - sheet and strip - determination of biaxial stress-strain curve by means of bulge test with optical measuring systems, 2014.

[47] J. Mulder, H. Vegter, H. Aretz, S. Keller, A.H. Van Den Boogaard, Accurate determination of flow curves using the bulge test with optical measuring systems, J. Mater. Process. Technol. 226 (2015) 169–187. doi:10.1016/j.jmatprotec.2015.06.034.

[48] L.C. Reis, P.A. Prates, M.C. Oliveira, A.D. Santos, J. V. Fernandes, Anisotropy and plastic flow in the circular bulge test, Int. J. Mech. Sci. 128–129 (2017) 70–93. doi:10.1016/j.ijmecsci.2017.04.007.

[49] J. Min, T.B. Stoughton, J.E. Carsley, B.E. Carlson, J. Lin, X. Gao, Accurate characterization of biaxial stress-strain response of sheet metal from bulge testing, Int. J. Plast. 94 (2017) 192–213. doi:10.1016/j.ijplas.2016.02.005.

[50] K. Chen, M. Scales, S. Kyriakides, E. Corona, Effects of anisotropy on material hardening and burst in the bulge test, Int. J. Solids Struct. 82 (2015) 70–84. doi:10.1016/j.ijsolstr.2015.12.012.

[51] S. Suttner, M. Merklein, Experimental and numerical investigation of a strain rate controlled hydraulic bulge test of sheet metal, J. Mater. Process. Technol. 235 (2016) 121–133. doi:10.1016/j.jmatprotec.2016.04.022.

[52] V. Livescu, J.F. Bingert, C. Liu, M.L. Lovato, B.M. Patterson, Biaxial deformation in high purity aluminum, Mater. Sci. Eng. A. 648 (2015) 330–339. doi:10.1016/j.msea.2015.09.086.

[53] J. Neggers, J.P.M. Hoefnagels, F. Hild, S. Roux, M.G.D. Geers, Direct Stress-Strain Measurements from Bulged Membranes Using Topography Image Correlation, Exp. Mech. 54 (2014) 717–727. doi:10.1007/s11340-013-9832-4.

[54] O. Paul, J. Gaspar, M. Engineering, Thin-Film Characterization Using the Bulge Test, in: Reliab. MEMS, Wiley- VCH Verlag GmbH & Co. KGaA, 2008: pp. 67–121. doi:10.1002/9783527622139.ch3.

[55] T.K. Tonge, L.S. Atlan, L.M. Voo, T.D. Nguyen, Full-field bulge test for planar anisotropic tissues: Part I-Experimental methods applied to human skin tissue, Acta Biomater. 9 (2013) 5913–5925. doi:10.1016/j.actbio.2012.11.035.

[56] C. Jayyosi, K. Bruyère-Garnier, M. Coret, Geometry of an inflated membrane in elliptic bulge tests: Evaluation of an ellipsoidal shape approximation by stereoscopic digital image correlation measurements, Med. Eng. Phys. 48 (2017) 150–157. doi:10.1016/j.medengphy.2017.06.020.

[57] D.W.A. Rees, Plastic flow in the elliptical bulge test, Int. J. Mech. Sci. 37 (1995) 373–

389. doi:10.1016/0020-7403(94)00071-Q.

[58] D.W.A. Rees, Sheet orientation and forming limits under diffuse necking, Appl. Math. Model. 20 (1996) 624–635. doi:10.1016/0307-904X(96)00010-8.

[59] A.R. Ragab, O.E. Habib, Determination of the Equivalent Stress, Mater. Sci. Eng. 64 (1984) 5–14.

[60] B.W. Williams, K.P. Boyle, Characterization of anisotropic yield surfaces for titanium sheet using hydrostatic bulging with elliptical dies, Int. J. Mech. Sci. 114 (2016) 315–329. doi:10.1016/j.ijmecsci.2016.05.022.

[61] M. Atkinson, Hydraulic bulging of near-isotropic sheet metal through an elliptical aperture, Int. J. Mech. Sci. 36 (1994) 247–255. doi:10.1016/0020-7403(94)90073-6.

[62] F. Abu-Farha, R. Verma, L.G. Hector, High temperature composite forming limit diagrams of four magnesium AZ31B sheets obtained by pneumatic stretching, J. Mater. Process. Technol. 212 (2012) 1414–1429. doi:10.1016/j.jmatprotec.2012.01.008.

[63] T. Zhu, M.A. Sutton, N. Li, J.J. Orteu, N. Cornille, X. Li, A.P. Reynolds, Quantitative Stereovision in a Scanning Electron Microscope, Exp. Mech. 51 (2011) 97–109. doi:10.1007/s11340-010-9378-7.

[64] A.D. Kammers, S. Daly, Digital Image Correlation under Scanning Electron Microscopy: Methodology and Validation, Exp. Mech. 53 (2013) 1743–1761. doi:10.1007/s11340-013-9782-x.

[65] J. Liao, J.A. Sousa, A.B. Lopes, X. Xue, F. Barlat, A.B. Pereira, Mechanical, microstructural behaviour and modelling of dual phase steels under complex deformation paths, Int. J. Plast. 93 (2017) 269–290. doi:10.1016/j.ijplas.2016.03.010.

[66] D. Banabic, H.-J. Bunge, K. Pöhlandt, a. E. Tekkaya, Formability of Metallic Materials, 2000. doi:10.1007/978-3-662-04013-3.

[67] G. Nolze, Image distortions in SEM and their influences on EBSD measurements, Ultramicroscopy. 107 (2007) 172–183. doi:10.1016/j.ultramic.2006.07.003.

[68] T.B. Britton, C. Maurice, R. Fortunier, J.H. Driver, A.P. Day, G. Meaden, D.J. Dingley, K. Mingard, A.J. Wilkinson, Factors affecting the accuracy of high resolution electron backscatter diffraction when using simulated patterns, Ultramicroscopy. 110 (2010) 1443–1453. doi:10.1016/j.ultramic.2010.08.001.

[69] C. Maurice, K. Dzieciol, R. Fortunier, A method for accurate localisation of EBSD pattern centres, Ultramicroscopy. 111 (2011) 140–148. doi:10.1016/j.ultramic.2010.10.007.

[70] F. Abu-Farha, X. Hu, X. Sun, Y. Ren, L.G. Hector, G. Thomas, T.W. Brown, In Situ Local Measurement of Austenite Mechanical Stability and Transformation Behavior in Third-Generation Advanced High-Strength Steels, Metall. Mater. Trans. A Phys. Metall. Mater. Sci. 49 (2018) 2583–2596. doi:10.1007/s11661-018-4660-x.

[71] T. Park, L.G. Hector, X. Hu, F. Abu-Farha, M.R. Fellinger, H. Kim, R. Esmaeilpour, F. Pourboghrat, Crystal Plasticity Modeling of 3rd Generation Multi-phase AHSS with Martensitic Transformation, Int. J. Plast. (2019). doi:10.1016/j.ijplas.2019.03.010.

[72] Q. SHI, S. Roux, F. Latourte, F. Hild, D. Loisnard, N. Brynaert, On the use of SEM correlative tools for in situ mechanical tests, Ultramicroscopy. 184 (2018) 71–87. doi:10.1016/j.ultramic.2017.08.005.